


Article

Development and Space Experiment Verification of Annular Liquid Flow Payload for China Space Station

Jia Wang^{1,2,†} , Yi Chen^{1,2,†}, Di Wu^{1,2}, Liang Hu¹, Zhijun Ye^{1,2}, Li Duan^{1,2,*}, Xilin Zhao³, Yongli Yin⁴ and Qi Kang^{1,2,*}

¹ Key Laboratory of Microgravity, Institute of Mechanics, Chinese Academy of Sciences, Beijing 100190, China; wangjia@imech.ac.cn (J.W.)

² School of Engineering Sciences, University of Chinese Academy of Sciences, Beijing 100049, China

³ Yantai Yuzhe Elect Technol Co., Ltd., Yantai 264005, China

⁴ Beijing HQJY R&T Co., Ltd., Beijing 100094, China

* Correspondence: duanli@imech.ac.cn (L.D.); kq@imech.ac.cn (Q.K.)

† These authors contributed equally to this work.

Abstract: The annular flow payload is among the first batch of space science experimental projects carried out on the Fluid Physics Rack of the China Space Station. This paper provides a detailed introduction to the development of the payload, ground validation, and in orbit experiments. The payload, sized 320 mm × 200 mm × 220 mm, includes an annular flow model and supports supply (24 V, 12 V, and 5 V), communication, and data transmission. A multi-functional heating column in the annular flow model was designed, allowing for the column to operate in fixed, rotating, and lifting scenarios. In the first round, 96 sets of space experiments covering volume ratio ranges from 0.45 to 1.06 were carried out. The annular flow liquid surface state, temperature oscillation, and infrared temperature field evolution were obtained. Mode decomposition shows the oscillatory convection of the $m = 4$ travelling wave, and contains $m = 3$, $m = 6$, and $m = 8$ waves.

Keywords: space experiment; annular liquid flow; payload development; thermocapillary convection; oscillatory instability



Citation: Wang, J.; Chen, Y.; Wu, D.; Hu, L.; Ye, Z.; Duan, L.; Zhao, X.; Yin, Y.; Kang, Q. Development and Space Experiment Verification of Annular Liquid Flow Payload for China Space Station. *Symmetry* **2024**, *16*, 1530. <https://doi.org/10.3390/sym16111530>

Academic Editor: Theodore E. Simos

Received: 14 October 2024

Revised: 1 November 2024

Accepted: 11 November 2024

Published: 15 November 2024



Copyright: © 2024 by the authors. Licensee MDPI, Basel, Switzerland. This article is an open access article distributed under the terms and conditions of the Creative Commons Attribution (CC BY) license (<https://creativecommons.org/licenses/by/4.0/>).

1. Introduction

With the rapid development of the semiconductor industry, the demand for high-quality crystal materials is growing rapidly. The Czochralski method (abbreviated as CZ method) is an important technology for preparing high-quality crystals. The annular flow is a typical spatial thermal convection model-derived therefrom. In space, the significant reduction in static pressure and buoyancy convection makes it possible to grow large-sized crystals. The spatial Cz method holds great industrial prospects and provides guidance for crystal growth by the ground pulling method. The non-uniform temperature distribution on the molten free surface forms a surface tension gradient that drives thermocapillary convection.

Early studies on annular flow focused on flow with a fixed central column. Sim et al. [1,2] obtained the relationship between the critical temperature difference and the liquid layer thickness when the thermocapillary convection flow turns unstable. Garnier et al. [3] observed spiral-shaped hydrothermal waves under two different liquid layer thickness conditions in ground experiments.

Kamotani et al. embarked on the thermocapillary convection experiment on United States Microgravity Laboratory-1 (USML-1), which was launched in June 1992 [4]. They built an inner heating and external cooling annular flow, using 10 cSt silicone oil as fluid medium. Two heating methods were employed, namely, laser heating (CF heating) and cylindrical heater heating (CT heating). Through numerical calculation and scaling analysis, the influence of heating method on the velocity field and temperature field was probed [5,6].

As only the steady state of thermocapillary convection was found in the first space experiment, they were subsequently dedicated to the second microgravity experiment in the USML-2 in order to research the oscillatory flow [7,8]. Researchers determined the oscillation initiation conditions, analyzed the velocity and temperature fields of the oscillating flow, and elucidated the importance of free surface deformation in the oscillation mechanism. It was discovered that a four-leaf pattern emerges in CF heating, and a rotating double-leaf pattern sometimes appears in CT heating [9]. In 2002, Schwabe and Benz et al. carried out observations of the flow transition process on the Russian FOTON-12 satellite [10,11]. They observed the spatiotemporal structure of thermocapillary flow under microgravity and measured the critical Marangoni number of the onset of oscillation. Various thermocapillary flow states are successfully observed under different conditions. At a small Marangoni number, a concentric multi-roll structure is presented, that is, co-rotating rolls are embedded in the main thermocapillary flow. As the Marangoni number increases, hydrothermal waves and complex oscillations appear. In addition, they also conducted an experimental study on convection in the Czochralski crucible. When the crystal rotation rate is higher than the critical value (about 0.1–0.2 r/s), the flow field transforms from laminar flow to baroclinically unstable oscillatory flow. The experiment shows that this flow field is almost linearly related to the temperature difference and significantly affected by the meniscus configuration [12,13].

In 2016, Kang et al. conducted a space experiment on annular flow, and they found that the critical oscillation curve of annular flow on a large curvature liquid surface is divided into two branches, “large volume ratio” and “small volume ratio”, confirming the volume ratio effect [14]. As the volume ratio increases, it shows a decreasing trend in the small volume ratio range and an increasing trend in the large volume ratio range. The flow instability begins with standing waves, which are transformed into traveling waves through competition, and then coupled with standing waves and traveling waves. The flow pattern is mainly transformed from wave number $m = 4$ to $m = 3$, which is related to the volume ratio [15]. A single bifurcation process of the second-frequency quasi-periodic oscillation and double-periodic oscillation was discovered [16].

In the process of crystal preparation, it is impossible to avoid the temperature difference between the melt and the crystal seed. The oscillation and transition characteristics caused by the coupling effect of thermocapillary convection and forced convection during the rotation and pulling process of the crystal seed, as well as suppressing the oscillation or transition of convection as much as possible, can avoid the occurrence of defects and ultimately improve the quality of crystal growth. A circular liquid pool with a center column that can be pulled and rotated was selected as the research model for studying annular flow [17,18]. Shi et al. [19–21] found that when the central column rotates at a relatively low speed, the propagation direction of the thermal fluid wave after flow instability is opposite to that of the rotation direction. As the rotation speed increases, the flow in the liquid pool also tends to be in a more unstable state. Zeng et al. [22,23] observed two oscillation modes of flow instability for crystal rotation and confirmed that thermocapillary force is the main cause of flow instability. Li et al. [24] considered the impact of rotation through linear stability analysis and numerical simulation. It was found that the propagation direction of the hydrothermal wave is opposite to the rotation direction of the liquid pool [25,26]. Even when the rotation speed is extremely low, it has a highly visible impact on the steady-state axisymmetric thermocapillary convection. Shen et al. [27] considered the influence of simultaneous rotation of the crystal and the crucible on the flow stability founding that when the two performed rotational motions in the same direction, the critical parameters for flow instability showed a trend of first decreasing and then increasing. Vasiliev et al. [28] found that the horizontal temperature difference in the rotating layer leads to the formation of convection with complex structures. Baroclinic waves provide most of the heat transfer at intermediate radii and lead to strong temperature and velocity fluctuations.

The study of annular flow needs benchmark data of the couple between the forced flow and thermocapillary flow. However, since most experiments are conducted on the

ground, the interference of buoyancy brings difficulties to studying the thermocapillary effect. Previously, there had been no annular flow experiments conducted that considered the complex coupling of the temperature gradient and the rotation and pulling process. The space environment provides a special platform for studying turbulence problems. Microgravity can not only provide the possibility for studying the coupling effect of pure thermocapillary convection and forced flow, but also bring new research topics such as interface turbulence, the deformed interface effect, and fluid management: (1) Interface turbulence focuses on the transition of thermocapillary convection as the Marangoni number increases. The bifurcation routes leading to chaos are extremely complex, and external conditions directly affect their development process. (2) Deformed interface concerns the influence of meniscus morphology on the interface tension-driven convection structure, oscillation, transition, and annular flow breakage under microgravity. (3) Fluid management is centered around the control of flow pattern by rotating or lifting, relying on the knowledge about the structural characteristics of the interface flow boundary layer and the flow instability mechanism. The research on annular flow and hydrothermal waves can provide a solid theoretical foundation for microgravity fluid management and its application.

2. Experimental Setup and Experimental Plan

2.1. Experimental Model

The annular flow model is an axisymmetric model. The central column is the hot end, and its temperature is denoted as T_H . The outer wall is the cold end, and its temperature is denoted as T_L . The middle channel between the central column and the outer wall is used to store the fluid working medium, silicone oil, as shown in Figure 1. When there is a temperature difference between the two ends, under the action of surface tension, the interface fluid flows from the hot end to the cold end. Following the law of mass conservation, the fluid at the bottom flows from the cold end to the hot end. Due to the wall effect, vortices are generated in the fluid during the flowing process. When the temperature difference ΔT ($\Delta T = T_H - T_L$) exceeds the critical temperature difference ΔT_c , the flow field experiences periodic oscillation. And as the temperature difference increases, the flow field structure changes, having radial, circumferential, and axial motion components, making the flow have a specific flow mode.

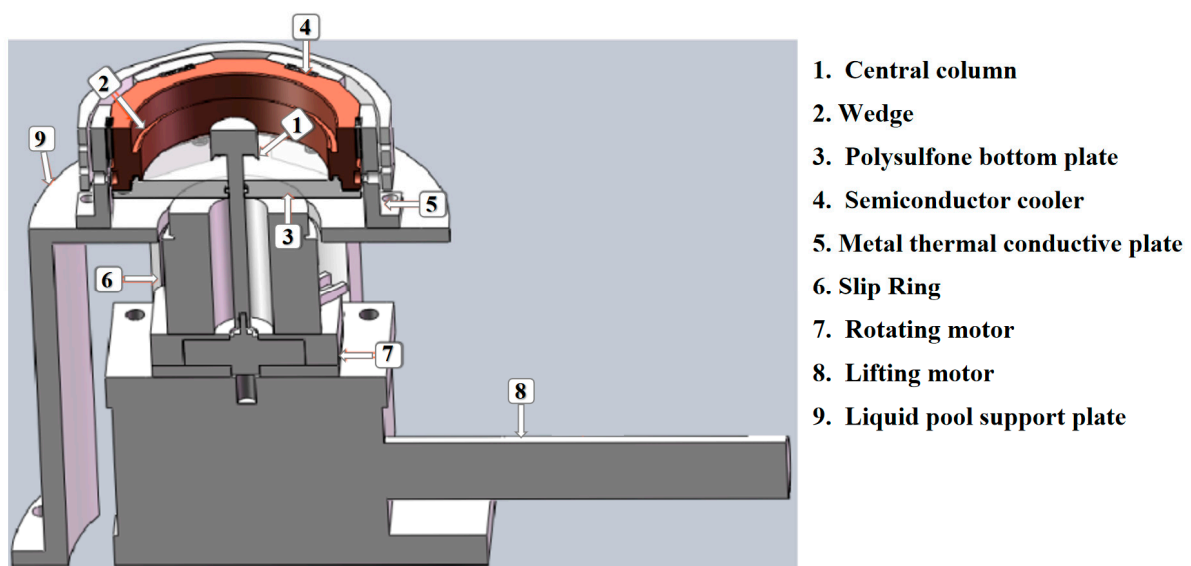


Figure 1. Annular liquid flow model.

Due to the action of surface tension and the change in liquid volume, the liquid has different initial interface stresses and becomes the flow complex. When the central column

rotates and Taylor–Couette flow is introduced, at this time, the flow field has the coupling effect of forced flow and thermocapillary convection. In the process of competition between flow mechanisms, the flow field exhibits more diverse flow characteristics and phenomena. By moving the axial position of the central column, the lifting of the central column can be achieved, that is, the influence of central binding force on convection can be studied. This physical model has the same function as the Cz method.

The specific parameters of the annular flow model are as follows (as shown in Table 1):

- (1) Outer radius of the liquid pool $R_o = 20$ mm, inner radius $R_i = 5$ mm, and depth $d = 12$ mm.
- (2) The central column of the liquid pool: The central column is a copper column with a heating film inside. The corresponding temperature is T_H and it is used to heat silicone oil.
- (3) The outer wall of the liquid pool: Made of copper, with six refrigeration chips attached on the outside, which can maintain the cold end at a relatively low temperature T_L .
- (4) Bottom surface of the liquid pool: Polysulfone plate.
- (5) Volume ratio V_r : 0.45–1.06.
- (6) Working medium: 2 cSt silicone oil (space experiment).

The boundary condition of the experiment is described as follows:

- (1) The inner boundary is the hold wall, which can rotate or lift.
- (2) The outer boundary is the cold wall, which is static.
- (3) The bottom boundary is a poor conductive wall.
- (4) The up boundary is a poorly conductive free surface, the Marangoni stress on which should be considered.

Table 1. Parameters of experimental space model.

Parameter	Value
Outer radius R_o	20 mm
Inner radius R_i	5 mm
Depth d	12 mm
Working medium	2 cSt silicone oil *
Volume ratio V_r	0.45~1.06
Temperature difference ΔT	0~35 °C

* For the physical properties of silicone oil, please refer to Table 2. The fluid working medium for the space experiment is 2 cSt silicone oil. The working mediums for the ground experiment are 1 cSt, 1.5 cSt, and 2 cSt silicone oil.

Table 2. Parameters experimental space model.

Silicone Oil (cSt)	Density ρ ($\text{kg}\cdot\text{m}^{-3}$)	Thermal Diffusion Coefficient κ ($\text{m}^2\cdot\text{s}^{-1}$)	Thermal Expansion Coefficient α (K^{-1})	Kinematic Viscosity ν ($\text{m}^2\cdot\text{s}^{-1}$)	Temperature Coefficient of Surface Tension σ_T ($\text{N}\cdot\text{m}^{-1}\text{K}^{-1}$)	Prandtl Number Pr
1 cSt	818	0.619×10^{-7}	1.29×10^{-3}	1.0×10^{-6}	-6.0×10^{-5}	16.16
1.5 cSt	852	0.595×10^{-7}	1.27×10^{-3}	1.5×10^{-6}	-6.0×10^{-5}	25.21
2 cSt	873	0.700×10^{-7}	1.24×10^{-3}	2.0×10^{-6}	-7.15×10^{-5}	28.10

2.2. Experimental Measurement System

The annular flow payload is a standard unit model of the fluid cabinet with a length, width, and height of 320 mm \times 200 mm \times 220 mm. It is placed in the fluid dynamics module of the Fluid Physics Rack. There is a circular observation window on the top of the liquid pool for observation by an infrared camera of the Fluid Physics Rack. There are three interfaces (X1, X2, and X3) on the front to complete power supply and communication with the Fluid Physics Rack. The internal structure and physical diagram of the experiment

equipment is shown in Figure 2. The payload has three power supply voltages of 24 V, 12 V, and 5 V, and can be communicated through RS422 and ethernet data transmission.

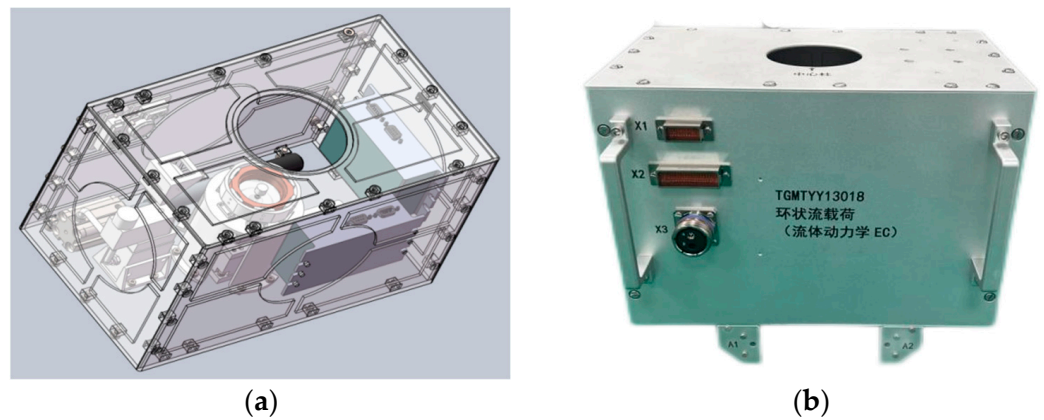


Figure 2. Annular liquid flow payload: (a) payload model diagram; (b) physical diagram of the payload.

The annular flow payload consists of eight parts, including the liquid pool, electrical control module, temperature control module, temperature acquisition module (thermocouple temperature acquisition and infrared temperature acquisition), rotation and lifting module, liquid injection and storage module, image acquisition module, and LED module, as shown in Figure 3. Among them, temperature control (controlled by the Eurotherm meter) and infrared temperature acquisition are provided by the Fluid Physics Rack. The PI motor inside the payload cooperates for the completion of liquid injection and suction. The camera observes the model establishment process and captures the interface morphology. The high-precision thermocouples collect the multi-phase temperature fluctuations inside the model. The lifting motor completes the lifting of the central column to form a pulling model. The rotating motor establishes forced convection. The payload uses the infrared camera of the Fluid Physics Rack to observe the liquid surface temperature. The Eurotherm meter completes the temperature control of the hot and cold ends of the model inside the payload. The spatial distribution positions of each part are shown in Figure 4.

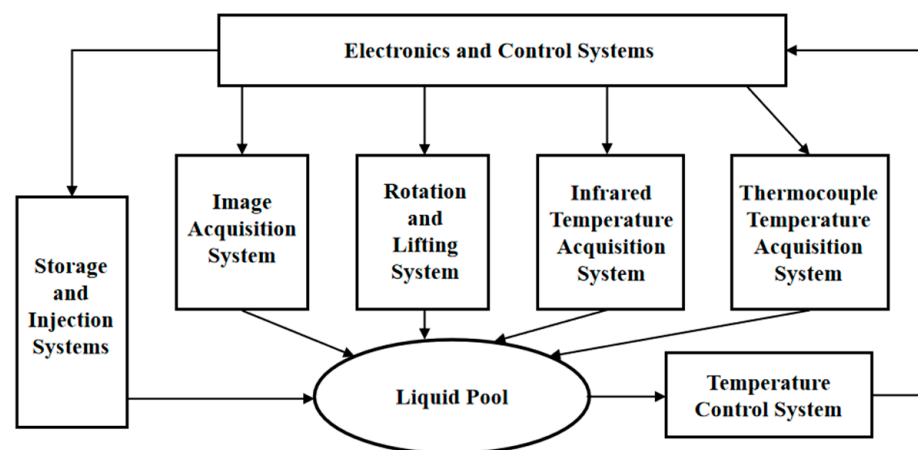


Figure 3. Composition of the annular flow payload system.

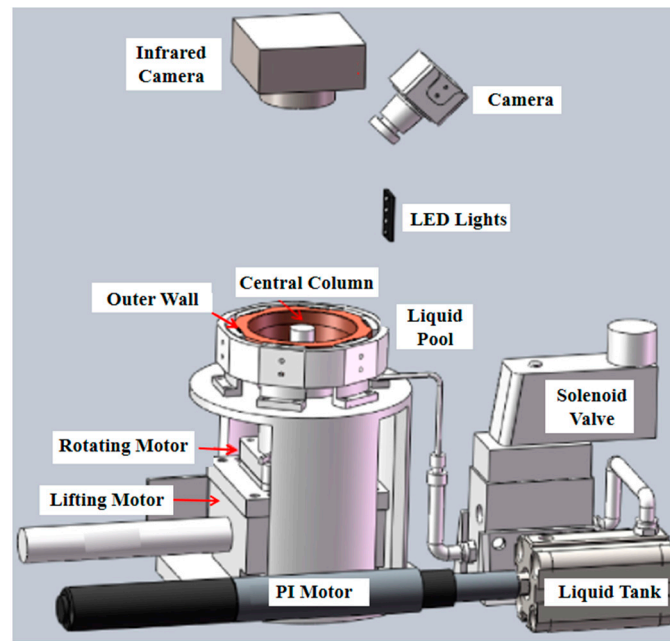


Figure 4. Internal structure of the annular flow payload.

2.2.1. Motors

The motors of the annular flow payload include three types of motors: injection motor, rotation motor, and lifting motor. The injection motor is a PI motor and is used to push the liquid cylinder and inject silicone oil into the liquid pool. The rotation motor is used to drive the central column to rotate and complete forced flow. The lifting motor pushes the central column to achieve movement in the vertical direction.

Injection Motor

The PI motor is connected to the piston of the liquid cylinder and injects silicone oil into the liquid pool from the injection hole. By controlling the relative position of the injection motor, experimental conditions with various volume ratios can be achieved. For relevant instruments and raw materials, etc., please refer to Appendix A Table A1 for details.

The M227 motor of PI company was selected. The stroke is 25 mm, and the minimum movable displacement is 0.05 μm . The space experiment program can realize the memory of the current position and the absolute position and can redefine the current position. Limiters (Festo, Esslingen, Germany, No 543862 SME-8M-DS-24V-K-2, 5-OE) are installed at both ends of the motor to avoid the motor running out of range due to incorrect instructions or other factors that result in jamming or failure.

Rotation Motor

The central column is connected to a rotation motor below. It is a 3709Z-12 type motor by the Lin Engineering Company (Morgan Hill, CA, USA). It is controlled by PWM control method (pulse width modulation). The speed can be adjusted from a few revolutions per second to more than ten revolutions per second, covering the working conditions required for space experiments. The rotation direction of the rotary motor can also be selected to achieve uniform rotation in both counterclockwise and clockwise directions, as shown in Figure 5.

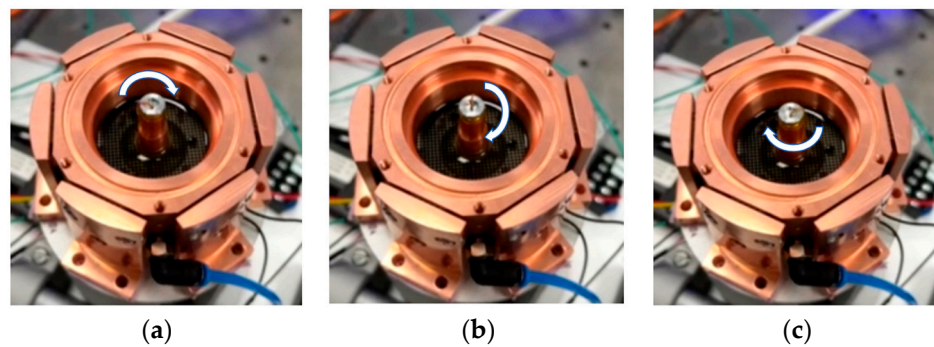


Figure 5. Central column rotates clockwise in ground experiment. The arrow indicates that the rotation direction of the central column is clockwise. (a) $t = \tau$; (b) $t = \tau + 1/4$ period; (c) $t = \tau + 1/2$ period.

Since the contact angle of silicone oil is extremely small, the liquid pool adopts a variety of protection designs. At the bottom and top of the central column and the top of the outer wall, wedge designs are adopted, and anti-climbing liquid is coated to ensure the stability of the liquid interface. The connecting rod between the central column and the rotation motor is covered with a sealing ring and a special-shaped sleeve to ensure no leakage during the rotation process, and the central column maintains stability and high coaxiality. A conductive slip ring is designed on the upper part of the rotary motor, which avoids the entanglement of thermocouples and wires during the rotation process.

By changing the voltage, rotation in clockwise and counterclockwise directions can be achieved, and fine adjustment of the rotation speed can also be realized.

The specific subdivision calculation is as follows:

Rotation speed calibration: w_P —planned rotation speed; w_R —actual rotation speed.

$$w_R = -0.01w_P^2 + 1.51w_P + 3.8 \quad (1)$$

PWM frequency setting.

Let the subdivision amount be s , the planned rotation speed be w_P (r/min), and the PWM frequency be f (Hz/s). Then the relationship between frequency and planned rotation speed is

$$f = w_P / 60 \cdot s \quad (2)$$

According to the rotation speed calibration relationship,

$$w_P = \frac{-1.51 \pm \sqrt{2.28 + 4 \cdot 0.01 \cdot (3.8 - w_R)}}{-0.02} \quad (3)$$

So, the relationship between frequency and actual rotation speed is

$$f = \frac{-1.51 \pm \sqrt{2.28 + 4 \cdot 0.01 \cdot (3.8 - w_R)}}{-1.2} \cdot s \quad (4)$$

The parameters of the motor are provided by the manufacturer.

The minimum rotation speed in the fitting section is 10 r/min, and the maximum rotation speed in the experiment is 55 r/min. The corresponding frequencies under each subdivision are as shown in Table 3.

Table 3. Subdivision amount correspondence table.

Subdivision Amount	Minimum Frequency	Maximum Frequency
200	14	171
400	28	342
800	56	685
1600	112	1371
3200	225	2742
6400	451	5484

Lifting Motor

The bottom of the central column of the annular flow is connected to a lifting motor. By controlling its lifting, the z-direction position of the central column can be changed, with a stroke of 0–15 mm, as shown in Figure 6. Through the subdivision algorithm, the slow and fast ascent and descent of the central column can be achieved. The speed control of the central column is stable, without tremors, jams, or other phenomena.

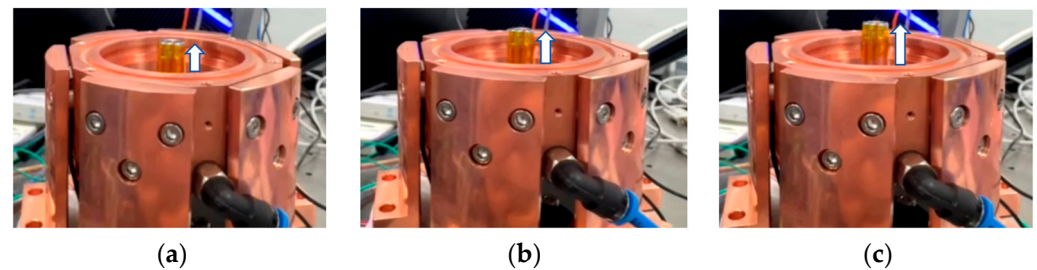


Figure 6. Central column rising process in ground experiment. The arrow indicates the movement direction of the central column, which is upward. (a) The height of the central column from the bottom of the pool is 3.53 mm; (b) The height of the central column from the bottom of the pool is 4.70 mm; (c) The height of the central column from the bottom of the pool is 5.56 mm.

The model of the lifting motor is PDV PT-GD75. Its stroke is 15 mm. The one-way positioning accuracy is ≤ 50 microns. The speed is ≤ 2 mm per second. The repeated positioning accuracy is ≤ 20 microns. The equivalent of pulse is 6043.341 (pulse value = $1/\tan(33.5)$ -driver pulse value). It comes with a photoelectric switch with an 8104 normally closed limit switch.

2.2.2. Liquid Storage Module

The silicone oil is stored in the liquid cylinder. The diameter of the piston in the liquid cylinder is 40 mm, and the length is 25 mm. The piston of the liquid cylinder is externally connected to a PI motor. The liquid outlet of the liquid cylinder is connected to the liquid inlet of the liquid pool via a solenoid valve. When the experiment starts, the solenoid valve is opened. After the PI motor moves to the specified position, the liquid injection is completed, and the solenoid valve is powered off.

2.2.3. Acquisition and Lighting

The payload is equipped with a camera. An LED light is placed under the camera to record the state of the liquid pool in real time. The camera resolution is 640×480 pixels, and real-time data transmission is completed through ethernet.

2.2.4. Temperature Control and Temperature Acquisition

Temperature control is composed of a temperature controller (a Eurotherm meter, provided by the Fluid Physics Rack) and thermocouples, and the PID (proportional–integral–derivative) algorithm is adopted. Two thermocouples are, respectively, used to measure the temperatures at the hot and cold end of the liquid pool and feed back to the Eurotherm meter to adjust linear heating or step heating.

2.3. Experimental Parameters

These factors are combined into non-dimensional parameters with different physical meanings to determine the flow state as follows:

Under the action of surface tension, the liquid interface presents a curved interface. Spatial experiments use the volume ratio to describe the interface morphology.

Volume ratio [14]:

$$Vr = V/V_0, \quad (5)$$

where V is the liquid volume and V_0 is the volume between the channels of the liquid pool [14]. Among them, the definition of V_0 is

$$V_0 = \pi(R_o^2 - R_i^2)d \quad (6)$$

Prandtl number [14]:

$$Pr = \frac{\nu}{\kappa}, \quad (7)$$

denoting the characterization of momentum flow and heat exchange in the fluid flow;

Marangoni number [14]:

$$Ma = \frac{\sigma_T(T_H - T_L)(R_o - R_i)}{\mu\kappa}, \quad (8)$$

which is used to characterize the driving effect of the surface tension, and the Marangoni number at the critical condition is commonly named as the critical Marangoni number, Ma_c .

The temperature dependency of the kinematic viscosity of the working fluid is evaluated from the following equation [14]:

$$\frac{\nu}{\nu_{25}} = \exp\left(5.892 \frac{25 - T}{273.15 + T}\right), \quad (9)$$

$$\nu = \frac{\nu(T_H) + \nu(T_L)}{2} \quad (10)$$

where ν_{25} is the kinematic viscosity at 25 °C and T is the temperature considered.

3. Ground Verification Experiment

In order to verify whether the payload has the functions and performance required for conducting on-orbit space experiments, payload ground experiments were carried out on the ground. In order to study the transition process from critical instability to chaos in ground experiments, thin liquid layer flows with a liquid layer thickness less than 4 mm were observed using 1 cSt, 1.5 cSt, and 2 cSt silicone oil as experimental working fluids, that is, thermocapillary convection with a volume ratio less than 0.30.

The cold end (T_L) is maintained at 1 °C lower than room temperature. The central column is controlled for linear heating to obtain the flow modes under different volume ratio conditions, and the heating rate is 0.5 °C/min. As the temperature difference increases, the flow instability problem of the transition from laminar flow to oscillatory flow as the temperature difference increases, as well as the influence of forced convection on flow instability. Therefore, two distinct flow states, namely, laminar flow state and oscillatory flow state, are obtained in ground experiments.

- (1) The laminar flow state is a centrally axisymmetric circulation. As the middle of the annular liquid pool is heated, the thermocapillary effect causes the surface fluid flow to the outside in an axisymmetric form, and the fluid at the bottom flows to the center, forming an axisymmetric circulation.
- (2) The oscillatory state is spontaneous oscillation caused by flow instability, which is manifested as a hydrothermal wave; see Figure 7. The colors represent the changes in temperature. In infrared images, red represents high temperature, while blue

represents low temperature. The hexagon formed by white dotted lines represents that the wave number of the hydrothermal waves are $m = 3$ (Figure 7a), 4 (Figure 7c), 5 (Figure 7e), and 6 (Figure 7g). Since there is coupling between the velocity field and the temperature field of thermocapillary convection, and its velocity also presents a similar wave structure. Therefore, the state of oscillatory flow is characterized by the fluctuation of surface temperature.

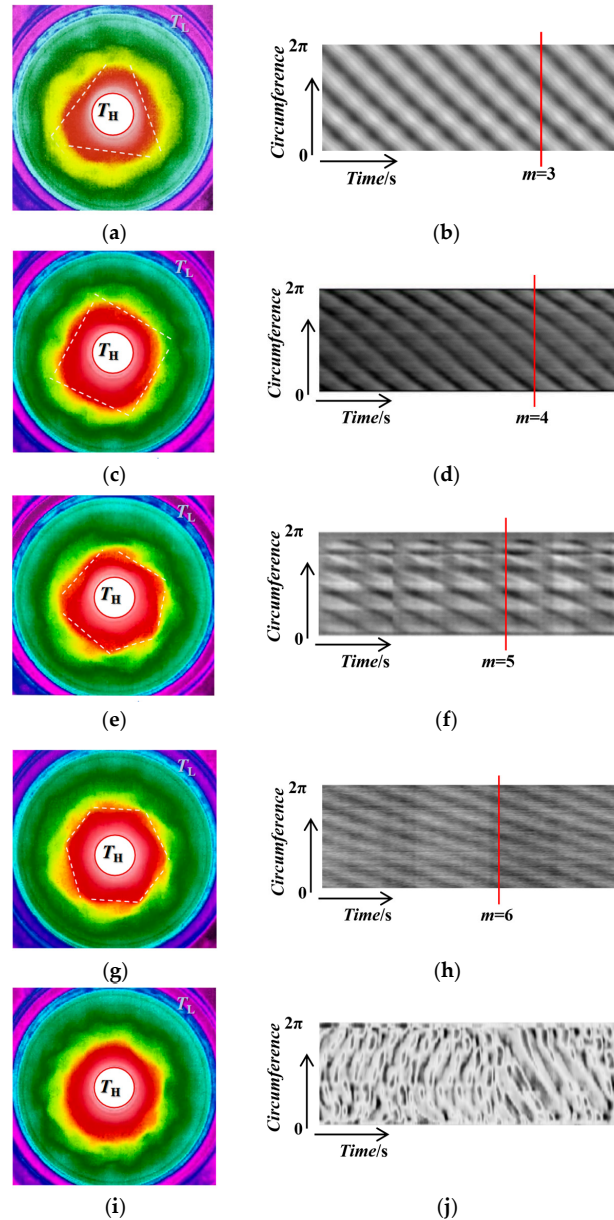


Figure 7. Infrared images of HTWs with different wave numbers in ground experiment. (a) HTWs with $m = 3$, $Vr = 0.2, 1.5$ cSt, $\Delta T = T_H - T_L = 36^\circ\text{C} - 12^\circ\text{C} = 24^\circ\text{C}$; (b) the corresponding circumferential temperature time evolution of (a); (c) HTWs with $m = 4$, $Vr = 0.15, 1.5$ cSt, $\Delta T = T_H - T_L = 30^\circ\text{C} - 10^\circ\text{C} = 20^\circ\text{C}$; (d) the corresponding circumferential temperature time evolution of (c); (e) HTWs with $m = 5$, $Vr = 0.15, 1$ cSt, $\Delta T = T_H - T_L = 27^\circ\text{C} - 11^\circ\text{C} = 16^\circ\text{C}$; (f) the corresponding circumferential temperature time evolution of (e); (g) HTWs with $m = 6$, $Vr = 0.10, 1$ cSt, $\Delta T = T_H - T_L = 27^\circ\text{C} - 13^\circ\text{C} = 14^\circ\text{C}$; (h) the corresponding circumferential temperature time evolution of (g); (i) disordered waveform, $Vr = 0.15, 1$ cSt, $\Delta T = T_H - T_L = 60^\circ\text{C} - 15^\circ\text{C} = 45^\circ\text{C}$; (j) the corresponding circumferential temperature time evolution of (i).

By changing the volume ratio and temperature difference, hydrothermal waves with different wave numbers such as $m = 3, 4, 5,$ and 6 can be obtained. For the hydrothermal wave with a wave number of 3 , there are three cold and hot zones in the corresponding flow field (Figure 7a). The hot and cold zones are alternately distributed in the circumferential direction. Spatiotemporal evolution is analyzed to study the changes in the interface temperature field based on the time and space domain. It can decompose the flow evolution of hydrothermal waves radially and circumferentially and obtain the temperature situation of the flow field at a certain moment. Specific flow field detail information such as wave number and rotation direction can be determined. In the temperature-time evolution graph, the grayscale represents temperature, with white representing high temperature and black representing low temperature. According to the temperature-time evolution in the circumferential direction (Figure 7b), there are three waves alternating between light and dark, which are traveling waves propagating clockwise; that is, the flow has regular periodic fluctuations. When the wave number is 4 , the temperature field corresponds to four cold and hot zones (Figure 7c), and so on. As the temperature difference increases, the transition of waveforms such as standing waves and traveling waves can occur. When the temperature is high enough and reaches super- (high) critical conditions, the flow becomes disordered, and the pattern appears as a disordered waveform (Figure 7i). The corresponding temperature stripes become irregular in time domain movement (Figure 7j).

The most important point in crystal growth is the regulation of the flow field. In the annular flow model, the control of flow modes is achieved by adjusting the rotation of the central column. The quasi-equilibrium state is the result of the balance between annular flow forced convection and thermocapillary convection. When the central column rotates, it drives the silicone oil in the liquid pool to generate following flow and generates a vortex cell structure in the flow field, that is, the so-called Taylor–Couette flow. Under the action of surface tension and restraining force, by changing the temperature difference and the rotation speed of the central column, the flow mode changes. As shown in Figure 8, the red area $R0$ is an identification area made for facilitating the display of the rotation of the central column, and the arrow indicates that the central column rotates counterclockwise. Colors represent temperatures. Red represents high temperatures and blue represents low temperatures. When the temperature difference is $24\text{ }^{\circ}\text{C}$, the wave number of the flow field is $m = 6$. By controlling the central column to rotate counterclockwise at a speed of two revolutions per second, the flow field maintains the mode of $m = 6$, and the flow mode does not change with time. These phenomena indicate that the payload can establish a fluid physical model and successfully carry out the experimental process to obtain valid scientific data.

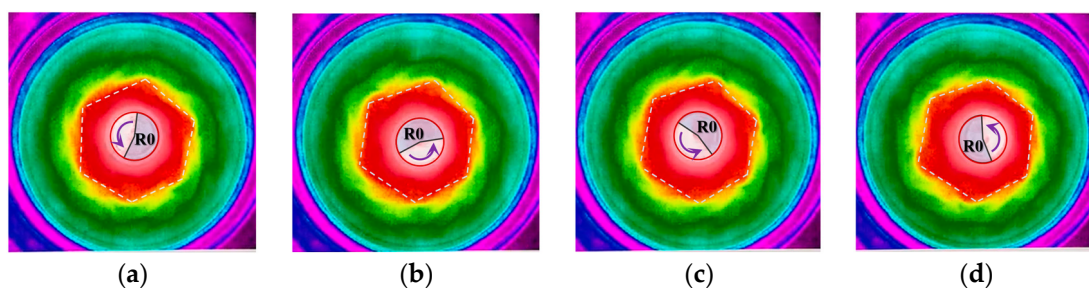


Figure 8. Quasi-equilibrium state, hydrothermal wave with $m = 6$, $Vr = 0.15$, 1 cst , $\Delta T = T_H - T_L = 26\text{ }^{\circ}\text{C} - 11\text{ }^{\circ}\text{C} = 15\text{ }^{\circ}\text{C}$. The time interval from (a) to (d) is 1 s . (a) $t = \tau$; (b) $t = \tau + 1\text{ s}$; (c) $t = \tau + 2\text{ s}$; (d) $t = \tau + 3\text{ s}$. The red area $R0$ is an identification area made for facilitating the display of the rotation of the central column.

4. Space Experiment Research and Result Analysis

The annular flow payload was installed on the Fluid Physics Rack by the Shenzhou-16 crew on 20 May 2023 (Figure 9). From June 2023 to November 2023, a total of six months of on-orbit experiments were conducted.

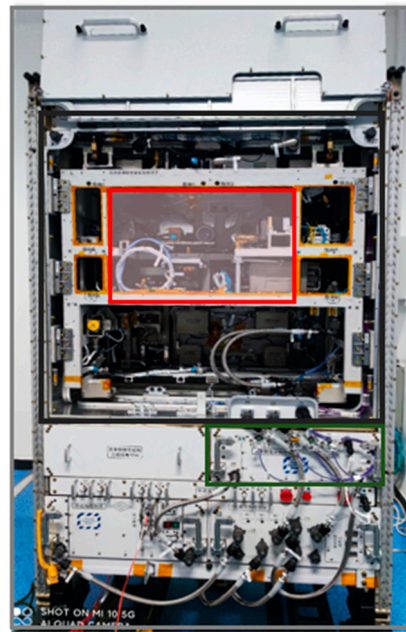


Figure 9. Installation of the annular flow payload in the fluid cabinet (red area).

Space experiments can issue experimental operations in the form of time-delay commands, real-time commands, or a combination of these two operations. Moreover, space experiments can be used to complete the injection of commands for multiple sets of working conditions at one time. Camera images, infrared images, and temperature oscillation signals can all be transmitted at high speed by the space station for real-time observation.

The process of a single space experiment is as follows (Figure 10):

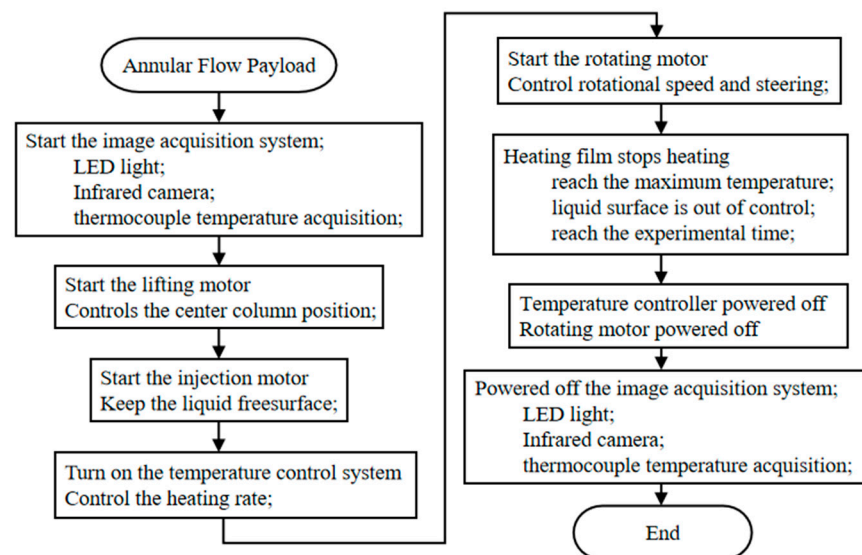


Figure 10. On-orbit experiment process of the annular flow payload.

- (1) Apply power to the payload through the Fluid Physics Rack.
- (2) Turn on the image acquisition system:
 - a. Turn on the LEDs;
 - b. Turn on the infrared camera of the Fluid Physics Rack. After waiting for it to start up, set the parameters and start acquisition;
 - c. Turn on the camera inside the payload for image acquisition.
- (3) Move the lifting motor to determine the position of the central column.

- (4) Turn on the PI motor and inject silicone oil into the liquid pool.
- (5) Set the high temperature T_H , low temperature T_L , and heating time t for the Eurotherm meter of the Fluid Physics Rack.
- (6) Start the rotating motor and set the rotation rate and direction.
- (7) The heating film and refrigeration chips start to work. When any of the following conditions is met, heating stops:
 - a. Reach the maximum high temperature;
 - b. Reach the heating time t ;
 - c. The fluid interface is out of control.
- (8) The heating film and refrigeration chips stop working, and the rotating motor stops working.
- (9) Turn off the image acquisition:
 - a. Turn off the LED lights;
 - b. Turn off the infrared camera;
 - c. Stop the temperature acquisition system.
- (10) Power off the payload and prepare to download the annular liquid flow payload scientific data.

The entire space experiment consists of independent single experiments, with the duration of a single experiment being 90 to 120 min. There are changes in parameters such as different volume ratios and heating modes. Each experiment is separated by 2–3 h. After the payload returns to the initial conditions (mainly referring to the temperatures of the central column and outer wall), the next experiment is carried out.

At present, a total of 96 sets of space experiments have been carried out, covering three types of convection model systems, including thermocapillary convection with a fixed central column, coupled Taylor–Couette flow and thermocapillary convection with a rotating central column, and convection under the lifting of the central column. The flow transition from steady instability to periodic motion and then to chaos and even turbulence was systematically studied. The evolution process of HTWs in different models in time and space domains was analyzed in depth.

Summary of experimental conditions.

- (1) Annular flow experiments of three physical models:
 - a. Experimental conditions with fixed central column: the volume ratio ranges from 0.45 to 1.06, with a total of 16 groups;
 - b. Experimental conditions with rotating central column: the volume ratio ranges from 0.80 to 1.00, with a total of 27 groups;
 - c. Experimental conditions with lifting central column: the volume ratio ranges from 0.90 to 1.00, with a total of eight groups.
- (2) Coverage of working conditions: volume ratio 0.45–1.00; temperature difference ΔT is larger than 25 °C.
- (3) Obtain data on convective instability and transition: infrared, thermocouple, and CCD image.

The results of annular flow space experiments mainly have three types of scientific data: temperature signals at a single point in the fluid, infrared images of the fluid interface, and high-definition images of the liquid surface morphology. In order to measure the instability of the annular flow, an infrared camera is used to collect the surface temperature, and thermocouples are used to collect the internal temperature as the main tool for measuring annular flow instability.

(1) Camera Images

With the assistance of camera images, the following tasks were achieved (as illustrated in Figure 11):

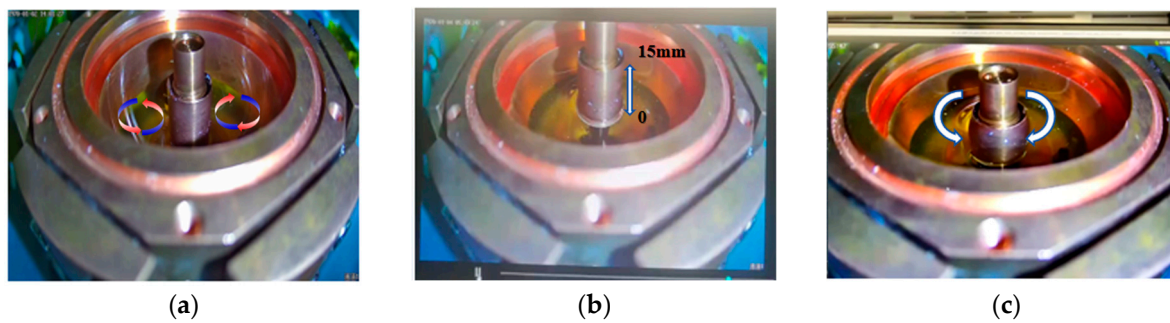


Figure 11. Annular liquid flow in space. (a) Fixed central column: on the free surface, under the action of surface tension, the liquid flows from the center to the side wall. Following the conservation of mass, the liquid at the bottom flows back to the central column from the side wall. (b) Central column lifting: it can be lifted from the bottom to 15 mm. (c) Central column rotation: it can move clockwise or counterclockwise.

In Figure 11a, the arrow indicates that the fluid flows from the hot end to the cold end at the interface, obeying the law of conservation of mass. Meanwhile, the liquid at the bottom flows from the cold end to the hot end. In Figure 11b, the arrow indicates that the central column can move vertically with a travel distance of 15 mm. In Figure 11c, the arrow indicates that in the on-orbit space experiment, the central column can rotate clockwise/counterclockwise.

Firstly, check whether the liquid injection is successful. By observing the interface morphology of the liquid in the liquid pool, we are able to determine whether the PI motor, solenoid valve, etc., are functioning properly and whether the instructions are executed in accordance with the process. Through observing the liquid surface, we can determine whether the liquid model has been set up.

Secondly, calculate the liquid volume ratio. As it is important to optimize the edge-extraction algorithm, we solve the Yang–Laplace equation to obtain the volume ratio, and the instruction parameters can be rectified through inversion. Previously, all volume ratio values were calculated based on the movement distance of the PI motor. Through CCD camera observation, the accuracy of volume ratio parameter can be guaranteed.

Thirdly, detect the establishment of the model. By observing the movement of the central column, we can qualitatively analyze the flow characteristics of Taylor–Couette flow, lifting model, etc.; monitor the climbing situation of the liquid surface; and preliminarily infer the scientific experiment results according to the free-surface reflection principle. This provides a basis for processing the experimental results and a reference for arranging subsequent scientific experiment conditions.

(2) Infrared Image Processing

The infrared camera can collect the temperature field of the free surface of the model in real time, which is important scientific data for annular flow space experiments. The infrared camera collects data at a frequency of 4 Hz and can accurately identify changes in the temperature field. Two main data processing methods are adopted for the infrared camera. One is spatiotemporal evolution (Figure 12), and the other is modal decomposition (Figure 13).

As shown in Figure 12, the infrared image shows a traveling wave of $m = 3$. However, through temperature time domain analysis, it can be known that the flow also has the characteristics of a standing wave at the same time, that is, an unstable traveling wave. When the temperature field is disturbed, the flow may transfer to another flow state.

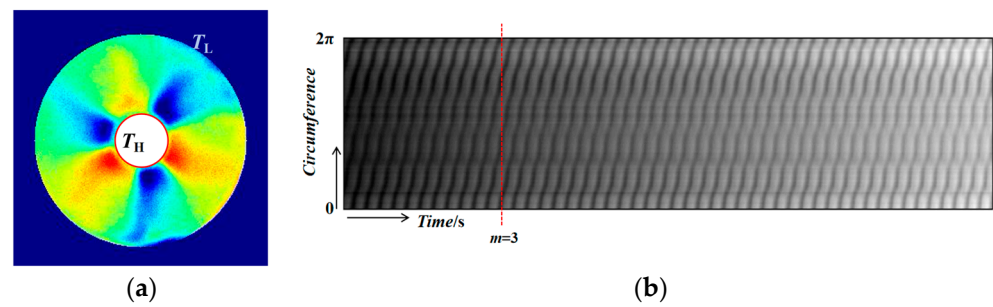


Figure 12. Temporal evolution of temperature (circumferential): (a) the infrared image after modal decomposition, $Vr = 1.05$, 2 cSt , $\Delta T = T_H - T_L = 44 \text{ }^\circ\text{C} - 24 \text{ }^\circ\text{C} = 20 \text{ }^\circ\text{C}$; (b) the corresponding circumferential temperature–time evolution.

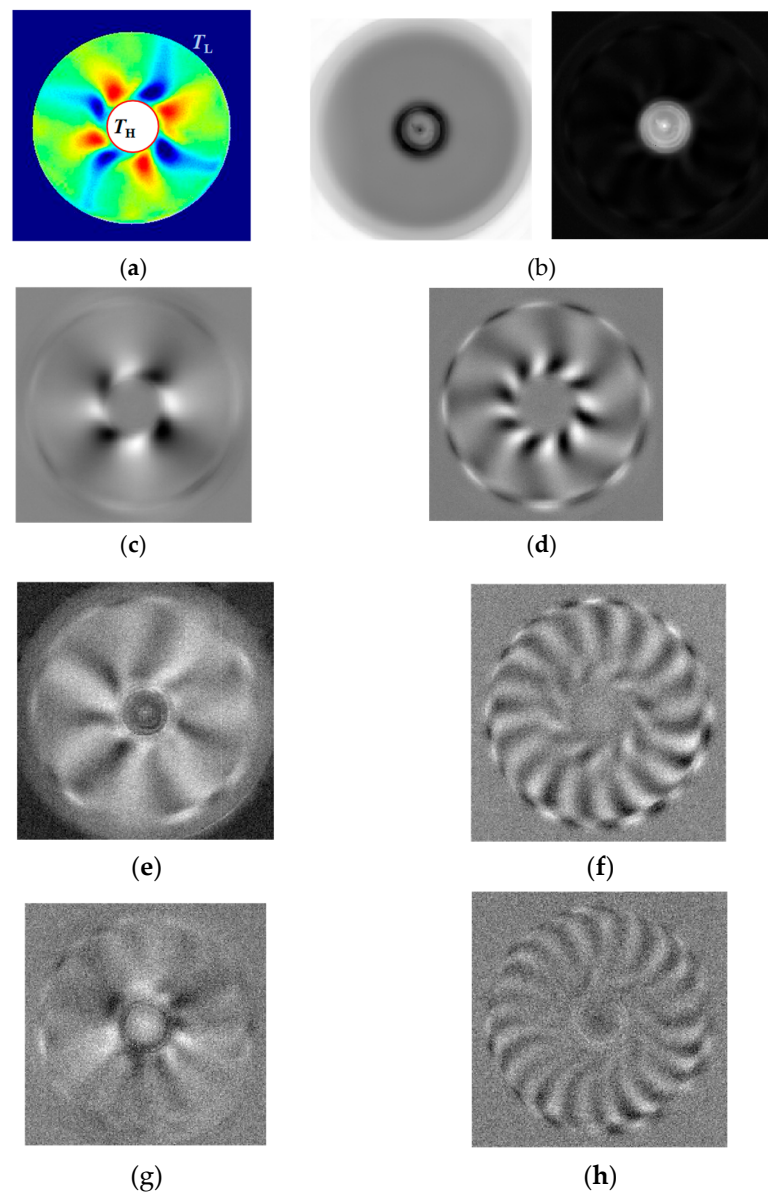


Figure 13. Modal decomposition of annular flow data (arranged according to the energy of HTWs), $Vr = 1.0$, 2 cSt , $\Delta T = T_H - T_L = 43 \text{ }^\circ\text{C} - 23 \text{ }^\circ\text{C} = 20 \text{ }^\circ\text{C}$. (a) Infrared disturbance image after subtracting the average value, $m = 4$; (b) infrared disturbance images during heating and cooling; (c) $m = 4$, traveling wave, clockwise; (d) $m = 8$, harmonic wave; (e) $m = 6$, harmonic wave; (f) $m = 8$, harmonic wave; (g) $m = 3$, harmonic wave; (h) $m = 8$, harmonic wave.

The evolution phenomenon indicates that there is a nonlinear process of multiple mode competitions in critical oscillation. To obtain the constituent components of the critical mode, the POD (proper orthogonal decomposition) method is adopted for the images data processing. The steps for POD method are as follows: (1) the temperature disturbance is calculated by subtracting the average distribution from the image sequence; (2) the data set $\Phi_{xt} = [I_1, I_2, \dots, I_n]$ is constructed by squeezing the 2D image to 1D vector I_i and rearranging them to a matrix; (3) singular value decomposition (SVD) is applied to the data set:

$$\Phi_{xt} = U \cdot S \cdot V^T \quad (11)$$

Herein, the column vectors in matrix V yield the modes of POD. The POD analyses extract the most dominant modes which are orthogonal to each other. Figure 13d shows the POD modes of instability process, in which plenty of modes are decomposed from the traveling wave of $m = 3$. Seemingly, a single mode actually contains multiple modes, $m = 3, 4, 6,$ and 8 , in the space experiment. As the heat of the fluid system continuously increases, a competition mechanism among modes emerges, breaking the existing balance. Some modes gradually decay, and the mode with $m = 3$ becomes dominant. The comparison between the space experiment and the ground test verifies that thermocapillary effect is the main mechanism that causes the oscillatory instability of the annular flow.

As shown in Figure 13, the infrared image shows a traveling wave with wave number $m = 4$. The ground test found waves of $m = 3, 4, 5,$ and 6 , which are basically consistent with the traveling wave phenomena in space experiments. Comparing with the ground test, the wave in microgravity is more regular, and the waveform presents a clear petal shape. After modal decomposition, according to the energy, it can be known that, in fact, the temperature field also contains standing waves of $m = 6$ and $m = 3$, as well as harmonics of $m = 8$. However, as time evolves, these waves gradually decay, and finally the flow field always presents a traveling wave state of $m = 4$.

(3) Thermocouple Temperature Signal Processing

Figure 14 shows the results of infrared images and thermocouples in the space experiment. The temperature measured by the thermocouple and the surface temperature field measured by the infrared camera both detected oscillations. This confirms that thermocapillary oscillations are not limited to the liquid surface but are a global flow instability.

At present, the research on chaos and turbulence of fluid is a long-term and challenging project. In a microgravity environment, the fluid is subject to relatively uniform forces in all directions. Chaotic flow can develop in a more symmetrical spatial structure, which helps to observe and study the essential characteristics of chaotic flow more clearly. Therefore, as an axisymmetric model, performing numerical analysis of chaotic dynamics on the nonlinear model of an annular liquid pool is a very good attempt.

As the temperature difference increases, the single-point temperature changes from non-oscillatory to oscillatory with a periodicity. When the temperature exceeds a certain value, the temperature fluctuation presents various transformation forms. And under the influence of rotational speed and direction, the flow correspondingly shows multiple modes.

Chaos is not a purely disordered state but an ordered motion state without periodicity and other obvious symmetry features. As the control parameters of a deterministic nonlinear system continuously change in a certain direction, when a certain limit state is reached, chaos, this aperiodic motion system appears. The system behavior of chaos often shows an infinitely nested self-similar structure. This structural similarity at different levels is invariant under scale transformation and reflects the law of chaotic motion. Chaotic attractors can characterize the separation degree of phase-space trajectories and the multi-dimensionality of spatial motion. As shown in Figure 15, when $r = (R_i + R_o)/2$ (point P_a), as the temperature difference increases, the flow shows relatively regular periodic oscillation, only with an increase in amplitude. Through three-dimensional sequence reconstruction, it can be seen that the motion trajectory continuously expands around a central axis. Using

the Wolf method to calculate the Lyapunov exponent to obtain $\lambda > 0$, it is confirmed that the flow has entered a chaotic state.

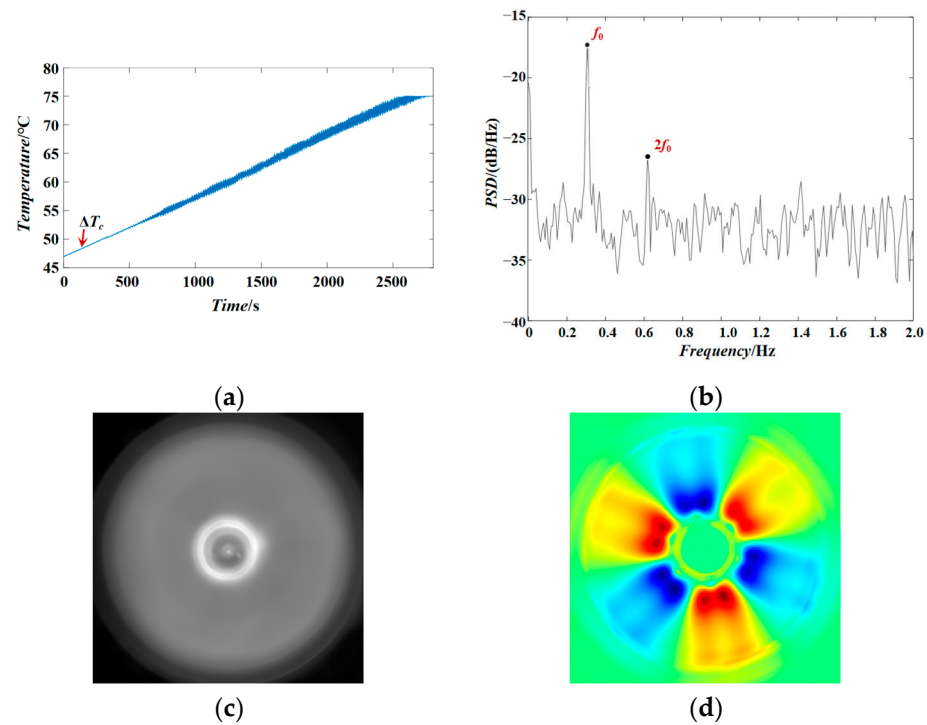


Figure 14. Annular flow space scientific data: (a) temperature data collected by thermocouples, and the arrow indicates the critical oscillation point; (b) frequency analysis of temperature data collected by thermocouples, the main frequency $f_0 = 0.30$ Hz; (c) original infrared image; (d) processed infrared image.

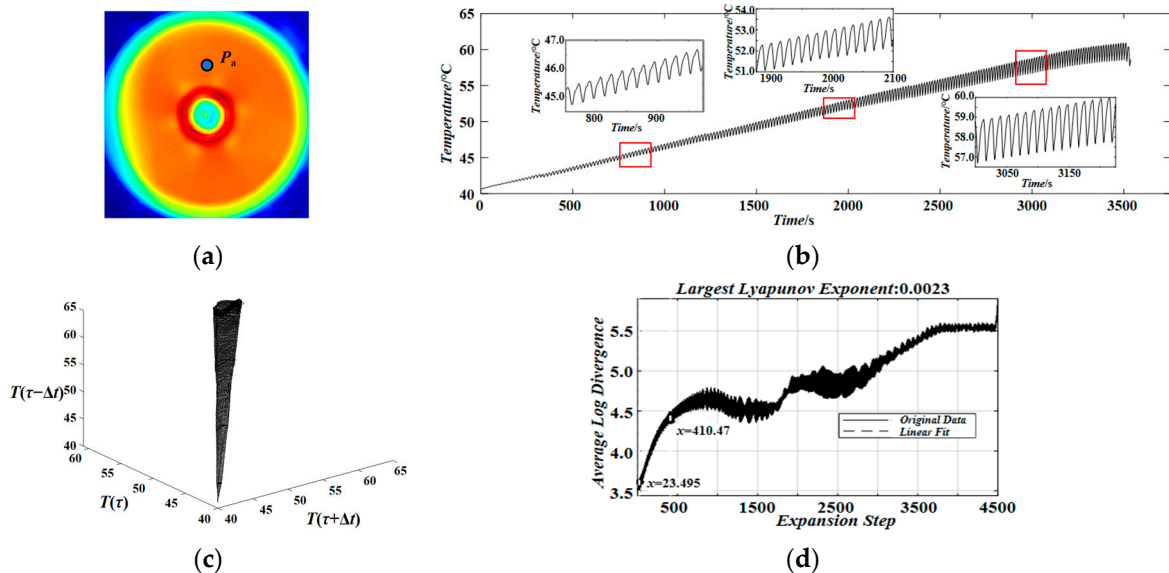


Figure 15. Chaotic attractor: (a) position of selected point, P_a ; (b) time histories of the temperature oscillations; (c) phase space reconstructions; (d) λ (Lyapunov exponent) calculation by the small data method. $T(\tau)$ is the temperature at time τ .

5. Conclusions

Annular flow is one of the first batch of scientific projects conducted on the Fluid Physic Rack in the China Space Station. Its aim is to research the oscillation characteristics and

transition problems of annular flow under microgravity. We introduced the implementation of this space experiment from two aspects: the payload development stage and the space experiment stage.

(1) Payload development and ground experiments

- To provide a fluid physic model for industrial crystal growth, a payload is developed, and ground experiments are finished. The experimental model of annular flow is constructed within the payload. This experimental model supports studying the thermocapillary convection and Taylor–Couette flow in microgravity. The thermocapillary convection is generated by heating the central column and maintaining the pool temperature, while Taylor–Couette flow is controlled by the rotation and lift of the column.
- In the ground test, a hydrothermal wave with different wave numbers such as $m = 3, 4, 5$, and 6 is observed in thermocapillary convection. A quasi-equilibrium state occurs at a certain temperature difference and rotation speed, and a static waveform is obtained through the balance between forced flow and thermocapillary convection.

(2) On-orbit experiments and findings

- On 20 May 2023, the Shenzhou-16 crew installed the annular flow payload on the Fluid Physics Rack. The payload executes the well-designed experimental process by using time-delay commands or real-time commands. During the first round of the space experiment, a total of six months of on-orbit experiments were carried out, and 96 sets of experiments were completed with different volume ratios, heating modes, and rotating modes.
- We have obtained scientific data such as images, thermocouple temperature signals, and infrared images. The CCD images verify that the annular flow has been successfully established, and that the injection of the working fluid, the maintenance of the interface, and the motion of the central column all function well.
- The spontaneous oscillation of the flow is simultaneously captured by thermocouples and the infrared camera. This indicates that the thermocapillary oscillation is a global instability that can be observed on the surface and in the bulk.
- We find that the transition from the $m = 4$ standing wave to the traveling wave exhibits a rich oscillation mode, including standing waves of $m = 6$ and $m = 3$, as well as harmonics of $m = 8$.

As a substantial quantity of space experiment data has been obtained, we will continuously conduct in-depth research on the instability mechanism of annular flow under microgravity conditions, including the onset of oscillatory flow, wave modes analysis, bifurcation to chaos, and so on. At the same time, we plan to conduct the second round of space experiment, which will concentrate on establishing a comprehensive understanding of the influence of volume ratio, rotation, and pulling state. Studying the flow evolution and control flow pattern in annular flow, for instance, oscillatory state or quasi-equilibrium state, will provide model and solution for crystal growth.

Author Contributions: Conceptualization, L.D. and Q.K.; methodology, L.D.; software, X.Z. and Y.Y.; validation, Z.Y., Y.C. and L.H.; formal analysis, D.W. and J.W.; investigation, J.W. and L.D.; resources, L.D. and Q.K.; data curation, J.W., Y.C. and D.W.; writing—original draft preparation, J.W.; writing—review and editing, J.W., Y.C. and L.D.; visualization, J.W., Y.C. and D.W.; supervision, L.D.; project administration, L.D.; funding acquisition, L.D. All authors have read and agreed to the published version of the manuscript.

Funding: This research was funded by the National Key R&D Program of China (Grant No. 2022YFF0503500) and the National Natural Science Foundation of China (Grant No. 12032020, 12072354, 12102438). Research on the Oscillation Characteristics and Transition Problem of Microgravity Annular liquid flow in Manned Space Station Program.

Data Availability Statement: Due to the confidentiality of the data, the original data are not provided in this paper.

Acknowledgments: Thanks to China Manned Space Engineering for providing space science and China Space Station application data products.

Conflicts of Interest: Author Xilin Zhao is employed by the Yantai Yuzhe Elect Technol Co., Ltd. Author Yongli Yin is employed by the Beijing HQJY R&T Co., Ltd. The remaining authors declare that the research was conducted in the absence of any commercial or financial relationships that could be construed as a potential conflict of interest.

Abbreviations

Full Term	Abbreviation
High temperature	T_H
Low temperature	T_L
Temperature difference	$\Delta T = T_H - T_L$
Outer radius of the pool	R_o
Inner radius of the pool	R_i
Depth	d
Volume ratio	$V_r = V/V_0$
Liquid volume	V
Pool volume	$V_0 = \pi(R_o^2 - R_i^2)d$
Density	ρ
Kinematic viscosity	ν
Thermal diffusion coefficient	κ
Coefficient of surface tension	σ
Temperature coefficient of surface tension	σ_T
Marangoni number	Ma
Prandtl number	Pr
Planned rotation speed	w_P
Actual rotation speed	w_R
Subdivision amount	s
PWM frequency	f
Wave number	m
Lyapunov exponent	λ
Data set of images	Φ_{xt}

Appendix A

Table A1. Summary of Material/Equipment.

Name of Material/Equipment	Company	Catalog Number	Comments/Description
Infrared camera	FLIR, Portland, OR, USA	Tau2	The diameters of the bare wires are 0.08 mm and 0.127 mm.
Thermocouples, K-type	North University of China, Taiyuan, China	ZBDX-HTTK	
Camera	WATTEC, East Flanders, Belgium	WAT-30HD	
Hydraulic cylinder	FESTO, Esslingen, Germany	ADVU-40-25-P-A	Diameter: 20 mm. Stroke: 0–25 mm. Controller: PI C-863.
Motor	PI, Karlsruhe, Germany	M-227	Measuring range: 25 mm. Stroke: 0–25 mm. Minimum displacement: 0.05 μm
Solenoid valve	FESTO, Esslingen, Germany	MFH-2-M5	
Pipe, 4 mm	FESTO, Esslingen, Germany	PUN-4X0,75-GE	
Heating film	HongYu, Beijing, China	125 Q/W335.1A	
Semiconductor Cooler	Zhongke, Tianjin, China	9502/065/021M	
LED	693 Institute, Beijing, China	10257MW7C	

Table A1. Cont.

Name of Material/Equipment	Company	Catalog Number	Comments/Description
Lifting motor	PDV, Beijing, China	PT-GD75	Stroke: 0–15 mm Speed ≤ 2 mm/s Accuracy ≤ 50 μm Repeated accuracy ≤ 20 μm
Rotation motor	Lin engineering Company, Morgan Hill, CA, USA	3709Z-12	Speed ≤ 2 mm/s maximum rotation speed: 55 r/min

References

1. Sim, B.C.; Zebib, A. Effect of free surface heat loss and rotation on transition to oscillatory thermocapillary convection. *Phys. Fluids* **2002**, *14*, 225–231. [\[CrossRef\]](#)
2. Limbourg, M.C.; Legros, J.C.; Petre, G. The influence of a surface tension minimum on the convective motion of a fluid in microgravity (D1 mission results). *Adv. Space Res.* **1986**, *6*, 35–39. [\[CrossRef\]](#)
3. Garnier, N.; Chiffaudel, A. Two dimensional hydrothermal waves in an extended cylindrical vessel. *Eur. Phys. J. B* **2001**, *19*, 87–95. [\[CrossRef\]](#)
4. Kamotani, Y.; Ostrach, S.; Pline, A. A thermocapillary convection experiment in microgravity. *ASME J. Heat Mass Transf.* **1995**, *117*, 611–618. [\[CrossRef\]](#)
5. Kamotani, Y.; Chang, A.; Ostrach, S. Effects of heating mode on steady antisymmetric thermocapillary flows in microgravity. *ASME J. Heat Mass Transf.* **1994**, *290*, 53–59.
6. Kamotani, Y.; Ostrach, S.; Pline, A. Analysis of velocity data taken in surface tension driven convection experiment in microgravity. *Phys. Fluids* **1994**, *6*, 3601–3609. [\[CrossRef\]](#)
7. Kamotani, Y.; Ostrach, S.; Pline, A. Some temperature field results from the thermocapillary flow experiment aboard USML-2 spacelab. *Adv. Space Res.* **1998**, *22*, 1189–1195. [\[CrossRef\]](#)
8. Kamotani, Y.; Ostrach, S.; Masud, J. Microgravity experiments and analysis of oscillatory thermocapillary flows in cylindrical containers. *J. Fluid Mech.* **2000**, *410*, 211–233. [\[CrossRef\]](#)
9. Kamotani, Y. Surface tension driven convection in microgravity. *Adv. Astronaut. Sci.* **1997**, *96*, 487–499.
10. Schwabe, D. Buoyant-thermocapillary and pure thermocapillary convective instabilities in Czochralski systems. *J. Cryst. Growth* **2002**, *237–239*, 1849–1853. [\[CrossRef\]](#)
11. Schwabe, D.; Benz, S. Thermocapillary flow instabilities in an annulus under microgravity—Results of the experiment magia. *Adv. Space Res.* **2002**, *29*, 629–638. [\[CrossRef\]](#)
12. Hintz, P.; Schwabe, D.; Wilke, H. Convection in a Czochralski crucible—Part 1: Non-rotating crystal. *J. Cryst. Growth* **2001**, *222*, 343–355. [\[CrossRef\]](#)
13. Hintz, P.; Schwabe, D. Convection in a Czochralski crucible—Part 2: Rotating crystal. *J. Cryst. Growth* **2001**, *222*, 356–364. [\[CrossRef\]](#)
14. Kang, Q.; Wang, J.; Duan, L.; Su, Y.Y.; He, J.W.; Wu, D.; Hu, W.R. The volume ratio effect on flow patterns and transition processes of thermocapillary convection. *J. Fluid Mech.* **2019**, *868*, 560–583. [\[CrossRef\]](#)
15. Kang, Q.; Wu, D.; Duan, L.; He, J.W.; Hu, L.; Duan, L.S.; Hu, W.R. Surface configurations and wave patterns of thermocapillary convection onboard the SJ10 satellite. *Phys. Fluids* **2019**, *31*, 20. [\[CrossRef\]](#)
16. Kang, Q.; Jiang, H.; Duan, L.; Zhang, C.; Hu, W.R. The critical condition and oscillation—Transition characteristics of thermocapillary convection in the space experiment on SJ-10 satellite. *Int. J. Heat Mass Transf.* **2019**, *135*, 479–490. [\[CrossRef\]](#)
17. Chen, Y.; Duan, L.; Kang, Q. Control of quasi-equilibrium state of annular flow through reinforcement learning. *Phys. Fluids* **2022**, *34*, 94105. [\[CrossRef\]](#)
18. Duan, L.S.; Duan, L.; Jiang, H.; Kang, Q. Oscillation Transition Routes of Buoyant Thermocapillary Convection in Annular Liquid Layers. *Microgravity Sci. Technol.* **2018**, *30*, 865–876. [\[CrossRef\]](#)
19. Shi, W.; Ermakov, M.K.; Imaishi, N. Effect of pool rotation on thermocapillary convection in shallow annular pool of silicone oil. *J. Cryst. Growth* **2006**, *294*, 474–485. [\[CrossRef\]](#)
20. Shi, W.; Li, Y.R.; Ermakov, M.K.; Imaishi, N. Stability of Thermocapillary Convection in Rotating Shallow Annular Pool of Silicon Melt. *Microgravity Sci. Technol.* **2010**, *22*, 315–320. [\[CrossRef\]](#)
21. Shi, W.Y.; Li, J.Y.; Wang, Y.; Li, Y.R. Numerical Analysis on Rotation-Thermocapillary Convection and Stability in Annular Pool of Silicon Melt. *J. Eng. Thermophys.* **2012**, *33*, 856–860.
22. Liu, H.; Zeng, Z.; Yin, L.; Qiu, Z.; Qiao, L. Effect of the crucible/crystal rotation on thermocapillary instability in a shallow Czochralski configuration. *Int. J. Therm. Sci.* **2019**, *137*, 500–507. [\[CrossRef\]](#)
23. Liu, H.; He, J.; Zeng, Z.; Qiu, Z. Instabilities of thermocapillary-buoyancy flow in a rotating annular pool for medium-Prandtl-number fluid. *Phys. Rev. E* **2021**, *104*, 035101. [\[CrossRef\]](#) [\[PubMed\]](#)
24. Li, Y.R.; Peng, L.; Wu, S.Y.; Zeng, D.L.; Imaishi, N. Thermocapillary convection in a differentially heated annular pool for moderate Prandtl number fluid. *Int. J. Therm. Sci.* **2004**, *43*, 587–593. [\[CrossRef\]](#)

25. Yu, J.J.; Li, Y.R.; Zhang, L.; Ye, S.; Wu, C.M. Experimental study on the flow instability of a binary mixture driven by rotation and surface-tension gradient in a shallow Czochralski configuration. *Int. J. Therm. Sci.* **2017**, *118*, 236–246. [[CrossRef](#)]
26. Wu, C.; Chen, J.; Li, Y. Mixed Oscillation Flow of Binary Fluid with Minus One Capillary Ratio in the Czochralski Crystal Growth Model. *Crystals* **2020**, *10*, 213. [[CrossRef](#)]
27. Shen, T.; Wu, C.-M.; Zhang, L.; Li, Y.-R. Experimental investigation on effects of crystal and crucible rotation on thermal convection in a model Czochralski configuration. *J. Cryst. Growth* **2016**, *438*, 55–62. [[CrossRef](#)]
28. Vasiliev, A.; Sukhanovskii, A.; Popova, E. Influence of Bottom Inclination on the Flow Structure in a Rotating Convective Layer. *Fluid Dyn. Mater. Process.* **2024**, *20*, 739–748. [[CrossRef](#)]

Disclaimer/Publisher’s Note: The statements, opinions and data contained in all publications are solely those of the individual author(s) and contributor(s) and not of MDPI and/or the editor(s). MDPI and/or the editor(s) disclaim responsibility for any injury to people or property resulting from any ideas, methods, instructions or products referred to in the content.